# Analysis of the through-focus images with boundary-element method in high resolution optical metrology

Deh-Ming Shyu and Mao-Hong Lu

Citation: Review of Scientific Instruments **77**, 103703 (2006); doi: 10.1063/1.2354570
View online: http://dx.doi.org/10.1063/1.2354570
View Table of Contents: http://scitation.aip.org/content/aip/journal/rsi/77/10?ver=pdfcov
Published by the AIP Publishing

# Analysis of the through-focus images with boundary-element method in high resolution optical metrology

Deh-Ming Shyu[a] and Mao-Hong Lu[b]
*Department of Photonics and Institute of Electro-Optical Engineering, National Chiao Tung University, 1001 Ta Hsueh Road, Hsinchu, Taiwan 300, Republic of China*

(Received 30 April 2006; accepted 23 August 2006; published online 5 October 2006)

For through-focus focus metric we build a measurement system, in which a single diffraction-limited micro lens is used for imaging and a grating with a few pitches is used as a target. In this system, the optical field is calculated by the boundary-element method, in which a new algorithm is developed to reduce the dimension of a matrix. As a result, the memory capacity required in this calculation is much reduced up to 83% in our simulation case. An optimization of the grating structure is made to obtain the highest sensitivity for the critical dimension metrology. With the optimized grating structure the simulation shows a sensitivity of less than 1 nm in the through-focus focus metric. © *2006 American Institute of Physics.* [DOI: 10.1063/1.2354570]

## I. INTRODUCTION

The development of the semiconductor industry has created the need for reliable critical dimension (CD) metrology. According to a developmental report of the semiconductor technology given by ITRS 2005 (International Technology Roadmap for Semiconductor), the physical gate length of 32 nm needs the gate CD control (accuracy) below 3.3 nm and CD metrology tool precision of 1.77 nm. Optical microscope is a general metrological tool for detecting the CD by imaging method at the best focal plane. However, if the CD is much smaller than the wavelength used in the optical microscope measurement, it is hard to measure the CD correctly because of the diffraction limit.[1,2] Recently the CD required in the semiconductor technology is very small (about 65 nm), so it becomes more and more difficult to satisfy the CD measuring requirement with imaging method.

Scatterometry[3–5] has been first proposed to measure the CD by using the grating-type target. The scattering light from the grating is very sensitive to the CD change of the feature size in the grating. However, the target size used in the scatterometer should be big enough to satisfy the condition of the theorem. If we need a small target to the CD metrology, the scatterometry will have a lot of problems. Thus, a through-focus focus-metric method[6–8] with optical microscope was proposed. The best focus position is determined by the autofocus algorithm. When the target is moved through focus, the optical image data are measured by a charge-coupled device (CCD) camera. The through-focus image data are analyzed by focus metric (FM) that gives the relation between the intensity distribution and the structure parameters of the grating-type target. This measurement system is inexpensive and analyzing by FM is not complicated.[9] In the through-focus focus-metric method, recently, the rigorous coupled-wave analysis[10–13] (RCWA) and the ray tracing are combined to simulate the through-focus images. A grating with a large number of pitches is required to satisfy the condition of RCWA, i.e., the dimension of the grating-type target must be big enough. Actually, the dimension of the target, bar in bar or box in box, in the fabrication is only about several micrometers and only contains a few pitches that cannot meet the condition of RCWA. Therefore, it is necessary to use another method to simulate the through-focus images for the CD metrology with optical microscope.

In this work, we simulate and analyze the optical microscope system for a grating with a few pitches by the boundary-element method (BEM).[14–17] Because the BEM is one of the boundary-type methods based on the integral-equation method, it can reduce the matrix dimension significantly in comparison with other domain-type methods, such as the finite element method[18] (FEM) or the finite-difference time-domain method (FDTD).[19,20] For the sake of simplification, in this system the optical microscope is made of one single microlens and a grating with five pitches is used as the target. In this case, the target is fixed and the image plane is moved through focus. A series of the images is taken and analyzed. The relation between the intensity distribution and the parameters of the grating linewidth, pitch, etc., has been found. In the analysis a change less than 1 nm in the CD can be resolved.

## II. ANALYSIS METHODS

### A. BEM for a six-region system

A schematic diagram of the optical microscope with a grating-type target of a few pitches is shown in Fig. 1. In this simulation, the lens in the optical microscope is a cylindrical lens. The wavelength used in this system is 0.45 $\mu$m. The whole space is divided into six homogeneous regions, $S_1$–$S_6$, separated by five boundaries, $\Gamma_1$–$\Gamma_5$. The image

[a]Electronic mail: sidney.eo89g@nctu.edu.tw
[b]Electronic mail: mhlu@cc.nctu.edu.tw

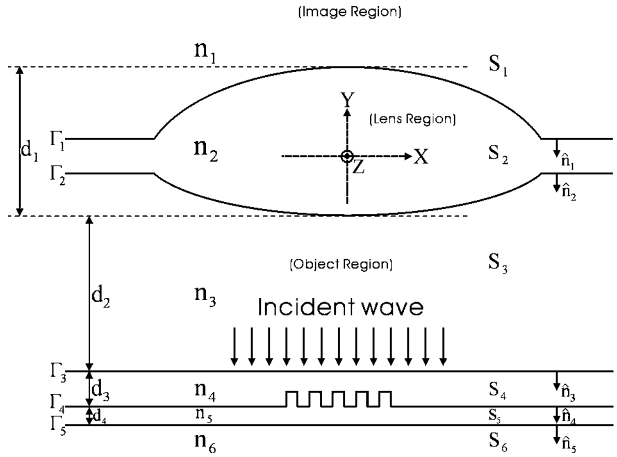


FIG. 1. Geometric structure of the optical system in simulation.

space is the region $S_1$. The object space contains three regions, $S_3$–$S_6$. The lens occupies the region $S_2$ with boundaries $\Gamma_1$ and $\Gamma_2$. The refractive index in region $S_i$ is denoted by $n_i$, $i=1,2,\ldots,6$. The refractive indices $n_1$, $n_3$, and $n_4$ are 1.0 (free space) in our simulation. The grating is formed by regions $S_5$ and $S_6$, where the region $S_5$ is the photoresist (PR) layer and the region $S_6$ is the substrate. A plane wave with unit amplitude is normally incident on the boundary $\Gamma_3$.

The boundary $\Gamma_3$ is a dummy boundary which does not have any effect on the optical field because the refractive indices in both sides are the same. The reflection field from the grating is focused and imaged by a cylindrical lens in the image region. By applying Green's theorem to Maxwell's equations and taking account of the radiation and boundary conditions, the regional integral equations can be expressed as[21]

$$\phi_1^t(r_1)+\int_{\Gamma_1}[\phi_{\Gamma_1}(r'_{\Gamma_1})\hat{n}_1\cdot\nabla G_1(r_1,r'_{\Gamma_1}) - p_1G_1(r_1,r'_{\Gamma_1})\psi_{\Gamma_1}(r'_{\Gamma_1})]d\ell'=0, \quad r_1\in S_1, \tag{1}$$

$$\phi_i^t(r_i)-\sum_{m=1}^{2}\int_{\Gamma_{(i-2)+m}}[\phi_{\Gamma_{(i-2)+m}}(r'_{\Gamma_{(i-2)+m}})\hat{n}_{(i-2)+m}\cdot\nabla G_i(r_i,r'_{\Gamma_{(i-2)+m}}) - p_iG_i(r_i,r'_{\Gamma_{(i-2)+m}})\psi_{\Gamma_{(i-2)+m}}(r'_{\Gamma_{(i-2)+m}})]d\ell' = \delta_i\cdot\phi^{inc}(r_i), \quad r_i\in S_i, \quad i=2,\ldots,5, \tag{2}$$

$$\phi_6^t(r_6)-\int_{\Gamma_5}[\phi_{\Gamma_5}(r'_{\Gamma_5})\hat{n}_5\cdot\nabla G_6(r_6,r'_{\Gamma_5}) - p_6G_6(r_6,r'_{\Gamma_5})\psi_{\Gamma_5}(r'_{\Gamma_5})]d\ell'=0, \quad r_6\in S_6, \tag{3}$$

with

$$G_i(r_i,r'_{\Gamma_{(i-2)+m}})=(-j/4)H_0^{(2)}(k_i|r_i-r'_{\Gamma_{(i-2)+m}}|), \tag{4}$$

$$i=1,2,\ldots,6.$$

Here $\phi=E_z$ and $p_i=1$ for TE mode and $\phi=H_z$ and $p_i=n_i^2$ for TM mode ($i=1,2,\ldots,6$). The $\phi^t$ and $\phi^{\text{inc}}$ are the total and the incident fields, respectively. $G_i$ is the two dimensional Green's function and $H_0^{(2)}$ is the zero-order Hankel function of the second kind. The vectors $r_i$ and $r'_{\Gamma_{(i-2)+m}}$ are the position vectors of points in region $S_i$ and on boundary $\Gamma_m$, respectively. $\delta_i$ is 1 if the source is in region $S_i$, otherwise $\delta_i$ is 0. In addition, the electromagnetic boundary conditions that must hold on boundary $\Gamma$ are (continuity of tangential electric field and magnetic field components)

$$\phi_{\Gamma_i}(r_{\Gamma_i})=\phi_i^t(r_{\Gamma_i})=\phi_{i+1}^t(r_{\Gamma_i}), \tag{5}$$

$$\psi_{\Gamma_i}(r_{\Gamma_i})=(1/p_i)\hat{n}_i\cdot\nabla\phi_i^t(r_{\Gamma_i})=(1/p_{i+1})\hat{n}_i\cdot\nabla\phi_{i+1}^t(r_{\Gamma_i}), \quad i=1,2,\ldots,5, \tag{6}$$

where $r_1$ denotes the coordinate of point on boundary $\Gamma_1$ in Eq. (1), $r_i$ is on boundaries $\Gamma_{i-1}$ and $\Gamma_i$ in Eq. (2) ($i=2,\ldots,5$), and $r_6$ is on boundary $\Gamma_5$ in Eq. (3). In this case the boundary integral equations can be divided by using a number of nodes on the boundaries $\Gamma_1$–$\Gamma_5$, and the fields at these nodes are determined by using the BEM with quadratic elements. From these values, at any point on the boundaries $\Gamma_i$ the field values $\phi_{\Gamma_i}$ and their derivatives $\psi_{\Gamma_i}$ can be calculated by quadratic interpolation. After the boundary values are known, the total field at any point $r_i$ in region $S_i$ can be determined by Eqs. (1)–(3).

### B. Reducing the dimension of matrix

In this section we propose a method to reduce the dimension of the matrix in the BEM. The memory needed in the computer for calculating the boundary solution is very large if many boundaries are included. For example, at least a 6 Gbytes memory is necessary if we have five boundaries and 1500 sampling points for each boundary. The memory capacity increases rapidly with the increase of the number of boundaries and sampling points. Thus, the BEM is difficult to be used if many boundaries are involved. The BEM for five boundaries and six regions can be represented in the matrix form[22]

$$\begin{bmatrix} H_{111} & -G_{111} & & & & & & & & \\ H_{211} & G_{211} & H_{221} & -G_{221} & & & & 0 & & \\ H_{212} & G_{212} & H_{222} & -G_{222} & & & & & & \\ & & H_{322} & G_{322} & H_{332} & -G_{332} & & & & \\ & & H_{323} & G_{323} & H_{333} & -G_{333} & & & & \\ & & & & H_{433} & G_{433} & H_{443} & -G_{443} & & \\ & & & & H_{434} & G_{434} & H_{444} & -G_{444} & & \\ & 0 & & & & & H_{544} & G_{544} & H_{554} & -G_{554} \\ & & & & & & H_{545} & G_{545} & H_{555} & -G_{555} \\ & & & & & & & & H_{655} & G_{655} \end{bmatrix} \begin{bmatrix} u_1 \\ q_1 \\ u_2 \\ q_2 \\ u_3 \\ q_3 \\ u_4 \\ q_4 \\ u_5 \\ q_5 \end{bmatrix} = \begin{bmatrix} -H_{111}u_{I1}+G_{111}q_{I1} \\ 0 \\ -H_{222}u_{I2}+G_{222}q_{I2} \\ 0 \\ -H_{333}u_{I3}+G_{333}q_{I3} \\ 0 \\ -H_{444}u_{I4}+G_{444}q_{I4} \\ 0 \\ -H_{555}u_{I5}+G_{555}q_{I5} \\ 0 \end{bmatrix}, \tag{7}$$

where the $H_{ijk}$ and $G_{ijk}$ are the submatrices. The suffixes $i$, $j$, and $k$ represent the submatrix in region $i$ and on boundary $j$ when the source point is on boundary $k$. The $u$ and $q$ are the potential and its outward normal derivative, respectively. The suffixes $m$ ($m=1,2,\ldots,5$) and $I$ in $u$ and $q$ stand for the boundary and input optical field, respectively. In our system, the input field is only on boundary 3, so the matrix elements in the right side of Eq. (7) are zero except the term $-H_{333}u_{I3}+G_{333}q_{I3}$. The quantities of $u_i$ and $q_i$ ($i=1,2\ldots,5$) can be easily obtained by using linear algebra to calculate Eq. (7). However, the matrix dimension is too large to calculate the inverse matrix directly. So we propose another inverse calculation method to solve Eq. (7). We can express Eq. (7) as follows:

$$\begin{bmatrix} M_{12} & M_{13} & 0 & 0 & 0 \\ M_{21} & M_{22} & M_{23} & 0 & 0 \\ 0 & M_{31} & M_{32} & M_{33} & 0 \\ 0 & 0 & M_{41} & M_{42} & M_{43} \\ 0 & 0 & 0 & M_{51} & M_{52} \end{bmatrix} \begin{bmatrix} UQ_1 \\ UQ_2 \\ UQ_3 \\ UQ_4 \\ UQ_5 \end{bmatrix} = \begin{bmatrix} UQ_{I1} \\ UQ_{I2} \\ UQ_{I3} \\ UQ_{I4} \\ UQ_{I5} \end{bmatrix}, \tag{8}$$

where

$$UQ_i = \begin{bmatrix} u_i \\ q_i \end{bmatrix}, \tag{9}$$

$$UQ_{Ii} = -H_{iii}u_I + G_{iii}q_I, \tag{10}$$

$$M_{i1} = \begin{bmatrix} H_{i(i-1)i} & G_{i(i-1)i} \\ 0 & 0 \end{bmatrix}, \tag{11}$$

$$M_{i2} = \begin{bmatrix} H_{iii} & -G_{iii} \\ H_{(i+1)ii} & G_{(i+1)ii} \end{bmatrix}, \tag{12}$$

$$M_{i3} = \begin{bmatrix} 0 & 0 \\ H_{(i+1)(i+1)i} & G_{(i+1)(i+1)i} \end{bmatrix}, \quad i=1,2,\ldots,5. \tag{13}$$

From Eq. (8), we have

$$M_{12}UQ_1 + M_{13}UQ_2 = UQ_{I1}, \tag{14}$$

$$M_{i1}UQ_{(i-1)} + M_{i2}UQ_i + M_{i3}UQ_{(i+1)} = UQ_{Ii}, \quad (i=2,3,4), \tag{15}$$

$$M_{51}UQ_4 + M_{52}UQ_5 = UQ_{I5}. \tag{16}$$

From Eq. (16), we can get

$$UQ_5 = T_{54}UQ_4 + A_{54}, \tag{17}$$

where

$$T_{54} = -\frac{M_{51}}{M_{52}}, \tag{18}$$

$$A_{54} = \frac{1}{M_{52}}UQ_{I5}. \tag{19}$$

Substituting $UQ_5$ into Eq. (15) ($i=4$), we have

$$UQ_4 = T_{43}UQ_3 + A_{43}, \tag{20}$$

and substituting $UQ_4$ into Eq. (15) ($i=3$), then we get $UQ_3$. Finally, substituting $UQ_3$ into Eq. (15) ($i=2$) we obtain $UQ_2$. So

$$UQ_i = T_{i(i-1)}UQ_{i-1} + A_{i(i-1)}, \quad (i=2,3,4), \tag{21}$$

where

$$T_{i(i-1)} = -\frac{M_{i1}}{M_{i2}+M_{i3}T_{(i+1)i}}, \tag{22}$$

$$A_{i(i-1)} = \frac{UQ_{Ii} - M_{i3}A_{(i+1)i}}{M_{i2}+M_{i3}T_{(i+1)i}}. \tag{23}$$

From Eqs. (14) and (21), we have

$$UQ_1 = \frac{UQ_{I1} - M_{13}A_{21}}{M_{12}+M_{13}T_{21}}. \tag{24}$$

The solution of $UQ_i$ ($i=1,2,\ldots,5$) can be solved easily. First, we obtain $UQ_1$ from Eq. (24) because the parameters $UQ_{I1}$, $M_{12}$, and $M_{13}$ are known. Moreover, the $T_{21}$ and $A_{21}$ can be gotten from $T_{i(i-1)}$ and $A_{i(i-1)}$ ($i=1,2,3,4$) according to Eqs. (22) and (23) if $T_{54}$ and $A_{54}$ are given by Eqs. (19) and (20). When the value of $UQ_1$ is obtained, all the $UQ_i$ ($i=1,2,\ldots,5$) can be obtained from Eq. (21). Because the inverse calculations are only in Eqs. (18), (19), (22), and

TABLE I. The parameters of cylindrical lens.

| Surface | Radius | Thickness ($\mu$m) | Refractive index | Half-width ($\mu$m) | Conic |
|---|---|---|---|---|---|
| Object | | 87.3 | | | |
| $\Gamma_2$ | −0.1020 | 70.0 | 2.0 | 70.0 | −0.5230 |
| $\Gamma_1$ | −0.5825 | 1230.0 | | 70.0 | 18.8417 |
| Image | | | | | |

(23), the needed memory capacity for the inverse calculations is decided only by the total number of sampling points and does not depend on the numbers of the boundaries. In this way the memory capacity needed in solving Eq. (7) is greatly reduced.

## III. LENS DESIGN

For the sake of simplification, the optical microscope is made of a single cylindrical microlens formed by two boundaries $\Gamma_1$ and $\Gamma_2$. The numerical aperture ($\mathrm{NA}_O$) in object space and magnification are 0.5 and 10×, respectively. The parameters of the cylindrical lens are listed in Table I. The lens surfaces $\Gamma_1$ and $\Gamma_2$ are described by function $\mathrm{sag}_y(x)$ that is expressed by Eq. (25).

$$\mathrm{sag}_y(x) = \frac{Cx^2}{1+\sqrt{1-(1+K)C^2x^2}}, \tag{25}$$

where $K$=conic constant and $C$=curvature=1/radius.

The thickness $d_1$ is 70 $\mu$m and the refractive index $n_2$ is assumed to be 2.0. The width of the cylindrical lens is 140 $\mu$m. The object and image distances are 87.3 and 1230.0 $\mu$m, respectively. The cylindrical lens is designed to be diffraction limited for the TE mode. The point spread function (PSF) of the cylindrical lens is simulated by BEM and shown in Fig. 2. The radius of the blur spot in Fig. 2 is about 4.0 $\mu$m which is the same as the value given by Eq. (26) without considering optical aberrations and polarization,

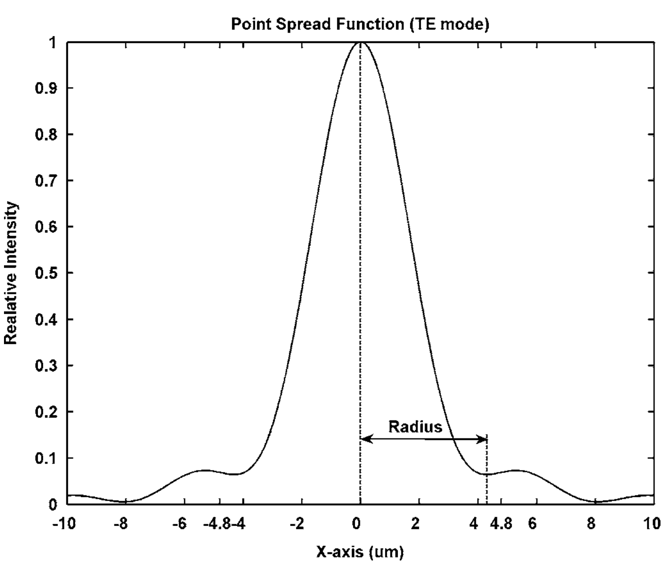


FIG. 2. The point spread function of the cylindrical lens.

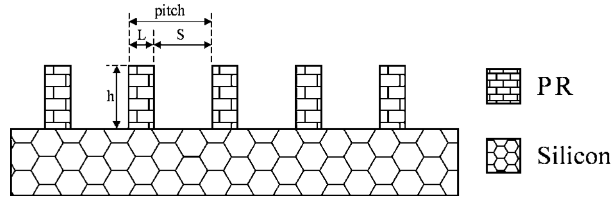


FIG. 3. Structure of the five-pitch linear grating.

$$r = \frac{0.5\lambda_0}{\mathrm{NA}_I}. \tag{26}$$

The wavelength $\lambda_0$ in free space and the numerical aperture in image space are 0.45 $\mu$m and 0.0572, respectively.

## IV. SIMULATION WITH BEM

A schematic diagram of the grating used as target is shown in Fig. 3. On a silicon substrate, a linear grating with five pitches is made of the PR. The geometric parameters of the grating are listed in Table II. The pitch and the $L/S$ ratio of the grating are 1.0 $\mu$m and 0.11, respectively. Both the width and height of the CD are 100 nm.

The grating in Fig. 3 contains three regions ($S_4$,$S_5$, and $S_6$) and two boundaries ($\Gamma_4$ and $\Gamma_5$) with the distance $d_4$ of zero, as shown in Fig. 1. The objective distance, the sum of $d_2$ and $d_3$, is 87.3 $\mu$m. In this simulation, we set the values of $d_2$ and $d_3$ as 87.0 and 0.3 $\mu$m, respectively. The input field is incident on the boundary $\Gamma_3$ with the width of 15 $\mu$m. The simulation result for the reflective field intensity of TE mode from the grating is shown in Fig. 4. The TE mode is more sensitive than the TM mode to the change in the dimension of CD, so we take TE mode in this simulation. From the simulation we can find that there are 0, ±1, and ±2 diffractive beams in the reflective field. Although only five-pitch grating is used, the diffraction properties of the grating are still obvious.

The grating as a target is imaged on an image plane by the cylindrical lens. The intensity distribution on the image plane which is moved through focus along the $y$ axis and at $z$=0 is shown in Fig. 5. We can see that the grating images appear at 1020, 1160, 1340, and 1600 $\mu$m on the $y$ axis and have a 180° phase difference between the adjoin images. For example, the line and space of the grating image at $y$=1160 $\mu$m are bright and dark, respectively, but at $y$ =1340 $\mu$m they are dark and bright, respectively. This result should be due to Talbot effect as mentioned in Ref. 23. The images of the grating at $y$=1250, 1300, and 1340 $\mu$m are shown in Fig. 6. The contrast of the image becomes higher when the position of the image approaches the best focal plane. It is difficult to image the CD directly because of the diffraction limit. Instead of the imaging method, the through-focus focus-metric method analyzes the optical field near the

TABLE II. Geometric parameters of the grating.

| | Material | $n$ | $k$ |
|---|---|---|---|
| Grating | PR | 1.574 53 | 0.002 017 |
| Substrate | Silicon | 3.867 | 0.020 |

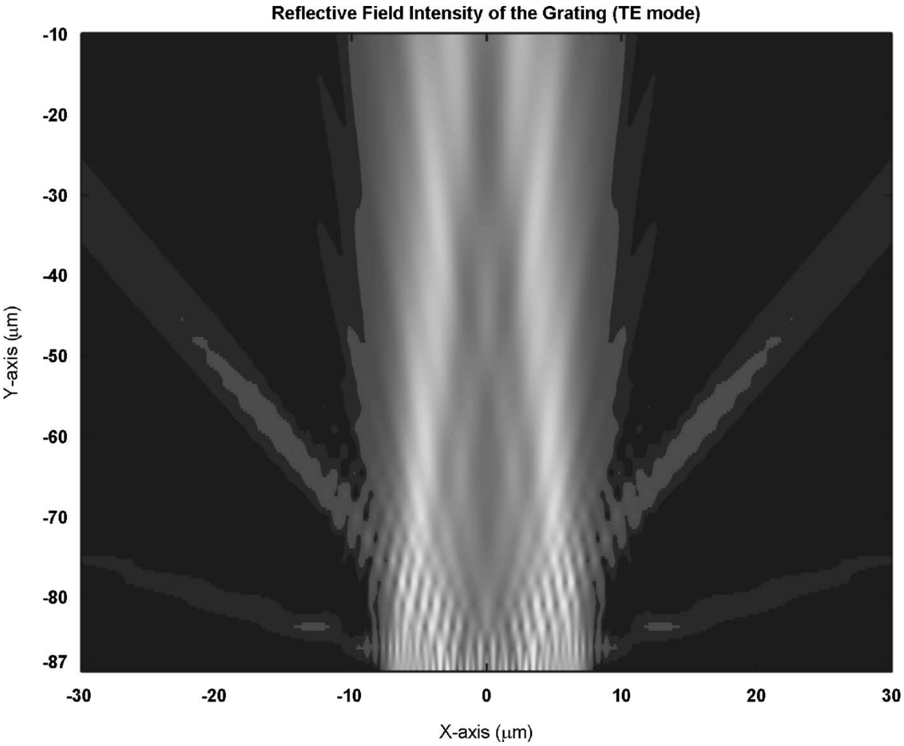


FIG. 4. The reflective field intensity of the grating.

best focal plane. We adopt three methods to describe the focus-metric signatures, i.e., gradient energy, standard deviation, and contrast. The gradient energy is defined as

$$\mathrm{FM_{GE}} = \frac{1}{m}\sum_{i=1}^{m} |\nabla f(x_i)|^2, \tag{27}$$

where $m$ is the total number of sample points, $\nabla$ is the, gradient operator and the, $f(x)$ is the intensity function on the $x$ axis. The standard deviation is formulated as

$$\mathrm{FM_{STD}} = \sqrt{\frac{\sum_{i=1}^{m} |f(x_i) - \bar{I}|^2}{m-1}}, \tag{28}$$

where $\bar{I}$ is the mean value of the intensity. The contrast is obtained from the minimum and maximum intensities and can be calculated as

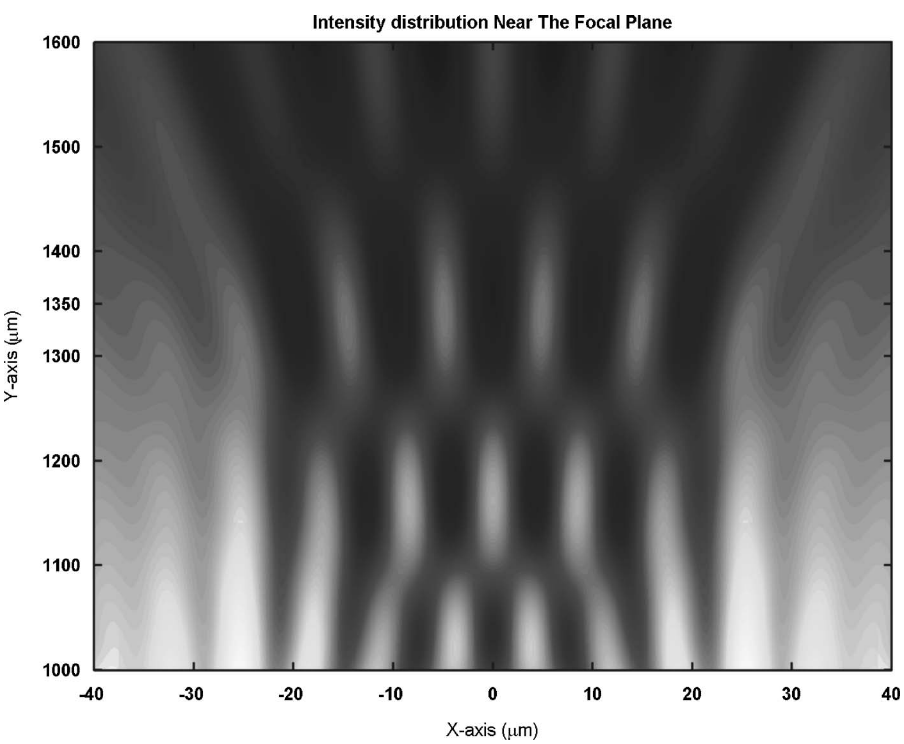


FIG. 5. Intensity distribution on the $x$-$y$ plane around the conjugate plane. The grating pitch is 1.0 $\mu$m and CD is 100 nm.

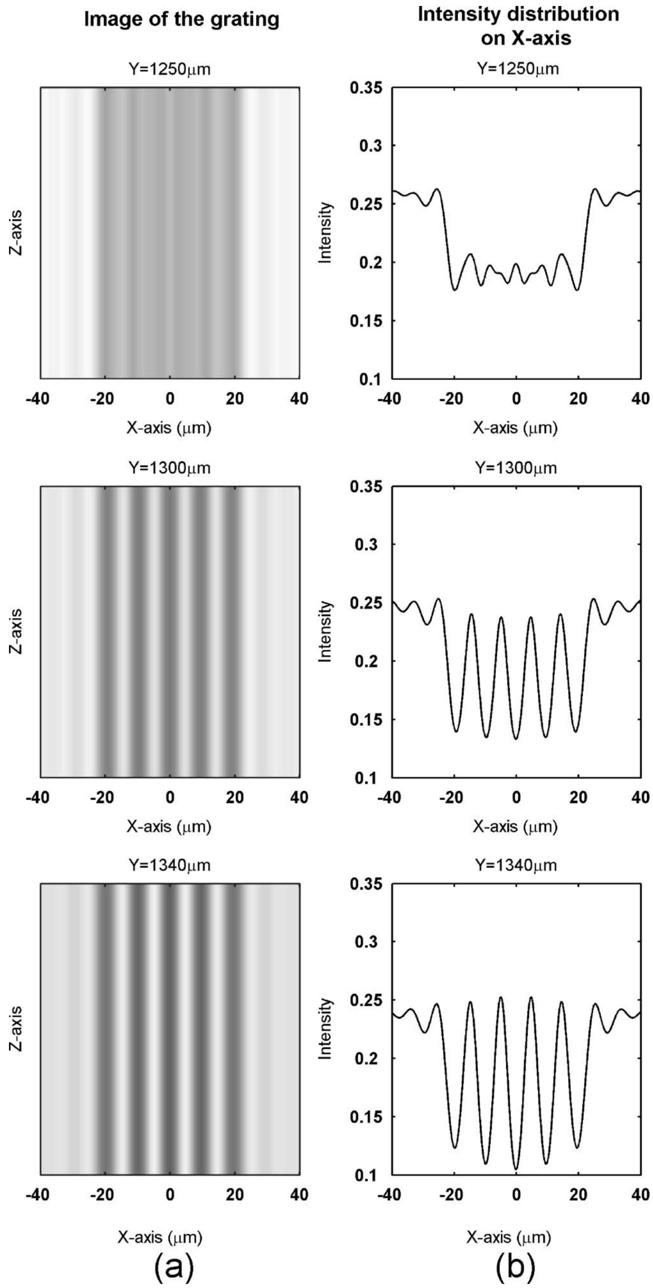


FIG. 6. (a) The images on different image planes and (b) the intensity distributions on the $x$ axis and at $z=0$. Here the image planes are at 1250, 1300, and 1340 $\mu$m on the $y$ axis.

$$\mathrm{FM}_{\mathrm{CTS}}=\frac{f(x)_{\max}-f(x)_{\min}}{f(x)_{\max}+f(x)_{\min}}, \tag{29}$$

where $f(x)_{\max}$ and $f(x)_{\min}$ are the maximum and minimum values of the intensity distribution. The calculation ranges of $x$ and $y$ in the intensity distribution of the image in through-focus focus-metric method are from −40 to 40 $\mu$m and from 1000 to 1600 $\mu$m, respectively. We have three kinds of the focus-metric signatures shown in Fig. 7, where the transverse coordinate represents the image position on the $y$ axis and the vertical coordinate represents the focus-metric values. In this calculation the pitch is 1.0 $\mu$m and the CDs are 90, 100, and 110 nm. The maximum variation in the focus-metric values for a variation of CD does not happen at the conjugate plane ($y=1300$ $\mu$m). From Fig. 7 we find that the signature

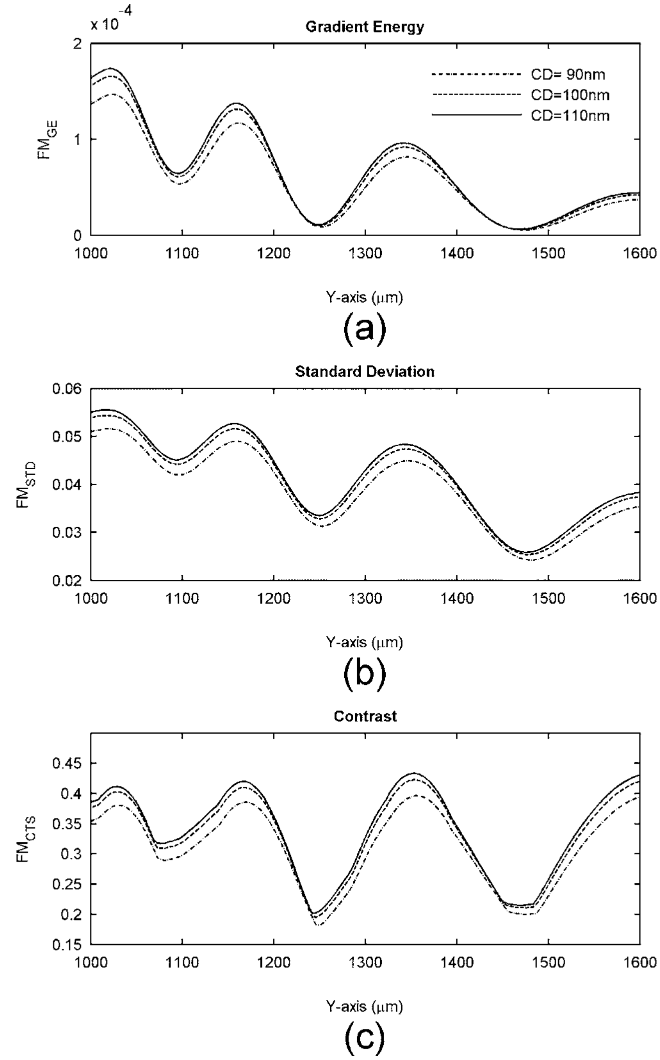


FIG. 7. Three kinds of the focus-metric signatures for (a) gradient energy, (b) standard deviation, and (c) contrast.

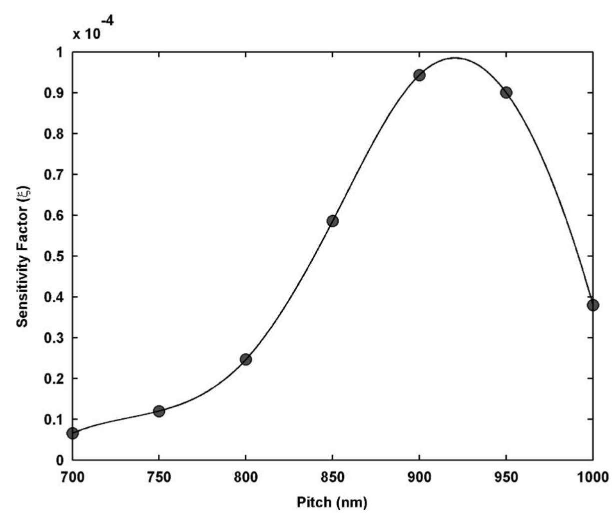


FIG. 8. The optimum for different pitches.

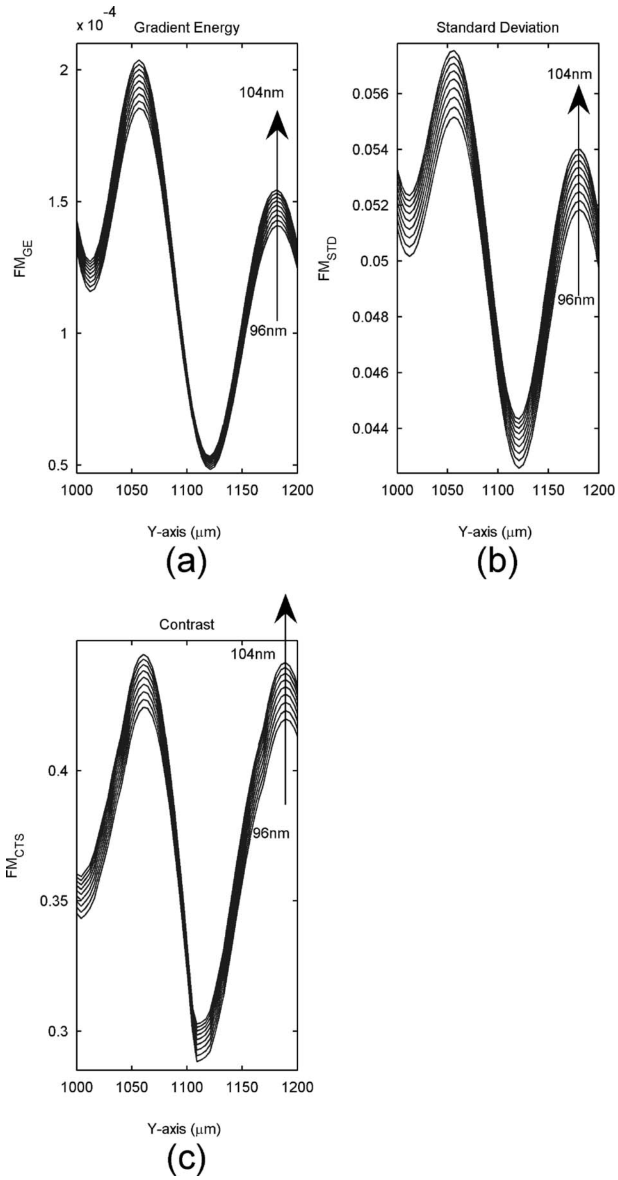


FIG. 9. Signatures at the optimum pitch of 920 nm for (a) gradient energy, (b) standard deviation, and (c) contrast.

for gradient energy is more sensitive than others. We optimize the pitch for higher sensitivity when the CD is fixed as 100 nm. We define a sensitivity factor $\xi$ as

$$\xi = \sqrt{\frac{\sum_{i=1}^{m} [\mathrm{FM_{GE}}(y_i,\mathrm{pitch},\mathrm{CD_1}) - \mathrm{FM_{GE}}(y_i,\mathrm{pitch},\mathrm{CD_2})]^2}{m|\mathrm{CD_1} - \mathrm{CD_2}|}}, \tag{30}$$

where $\mathrm{FM_{GE}}$ is the focus-metric value of gradient energy, which is a function of $y_i$, pitch, and $\mathrm{CD}_j$ $(j=1,2)$, and $m$ is the total number of sampling points. The $\mathrm{CD_1}$ and $\mathrm{CD_2}$ are $\mathrm{CD}+\Delta\mathrm{CD}$ and $\mathrm{CD}-\Delta\mathrm{CD}$, respectively. $\Delta$CD denotes the small variation of CD. The variation range of pitch in the optimization is from 700 to 1000 nm and the step is 50 nm. The CD is fixed as 100 nm and the $\Delta$CD is 5 nm. By calculating the sensitivity factor $\xi$ with Eq. (30), the results are shown in Fig. 8. Using interpolation method, we find the maximum value of $\xi$ to be at pitch of 920 nm. It means that a variation in the CD can be more sensitively detected if the pitch of the grating is 920 nm. The simulation results for the CD variation from 96 to 104 nm with step of 1 nm are shown in Fig. 9. From Fig. 9 we can see a change in the signatures for the CD variation, which is more sensitively detected in comparison with Fig. 7. The application of the through-focus focus-metric method to the optical microscope with the grating of a few pitches as the target is able to detect the CD variation below 1.0 nm. Therefore, we believe that using the optical microscope and analyzing the intensity distributions of the images in through focus to get the CD information is more convenient than other method.

[1] J. W. Goodman, *Introduction to Fourier Optics* (McGraw-Hill, New York, 1996), Chap. 6.
[2] H. E. Hwang, G. H. Yang, and J. C. Chou, Opt. Eng. (Bellingham) **41**, 2620 (2002).
[3] X. Niu, J. Opt. Soc. Am. A **5**, 1270 (1988).
[4] H. T. Huang, G. Raghavendra, A. Sezginer, and K. Johnson, Proc. SPIE **5038**, 126 (2003).
[5] W. Yang, L. W. Roger, and S. Rabello, Proc. SPIE **5038**, 200 (2003).
[6] Y. S. Ku, A. S. Liu, and N. Smith, Opt. Express **13**, 6699 (2005).
[7] R. M. Silver, R. Attota, M. Stocker, M. Bishop, J. Jun, and R. Larrabee, Proc. SPIE **5752**, 67 (2005).
[8] R. Attota, R. M. Silver, T. A. Germer, and M. Bishop, Proc. SPIE **5752**, 1441 (2005).
[9] M. Subbarao and J. K. Tyan, IEEE Trans. Pattern Anal. Mach. Intell. **20**, 864 (1998).
[10] N. Chateau and J. P. Hugonin, J. Opt. Soc. Am. A **11**, 1321 (1994).
[11] M. G. Moharam, E. B. Grann, and D. A. Pommet, J. Opt. Soc. Am. A **12**, 1068 (1995).
[12] T. K. Gaylord and M. G. Moharam, Proc. IEEE **73**, 894 (1985).
[13] E. N. Glytsis and T. K. Gaylord, J. Opt. Soc. Am. A **4**, 2061 (1987).
[14] J. S. Ye, B. Z. Dong, B. Y. Gu, G. Z. Yang, and S. T. Liu, J. Opt. Soc. Am. A **19**, 2030 (2002).
[15] J. S. Ye, B. Y. Gu, B. Z. Dong, and S. T. Liu, J. Opt. Soc. Am. A **22**, 862 (2005).
[16] K. Hirayama, E. N. Glytsis, and T. K. Gaylord, J. Opt. Soc. Am. A **14**, 907 (1997).
[17] Y. Nakata and M. Koshiba, J. Opt. Soc. Am. A **7**, 1494 (1990).
[18] J. E. Akin, *Application and Implementation of Finite Element Methods* (Academic, London, 1982).
[19] A. Taflove, *The Finite-Difference Time-Domain Method* (Artech House, Boston, 1995).
[20] R. Harrington, *Time-Harmonic Electromagnetic Fields* (McGraw-Hill, New York, 1961).
[21] K. Hirayama, K. Igarashi, and Y. Hayashi, J. Opt. Soc. Am. A **16**, 1494 (1999).
[22] S. Kagami and I. Fukai, IEEE Trans. Microwave Theory Tech. **32**, 455 (1984).
[23] H. F. Talbot, Philos. Mag. **9** 401 (1836).